Analyst

Near-infrared C2H2/CH4 dual-gas sensor system combining off-axis integrated-cavity output spectroscopy (OA-ICOS) and frequency-division-multiplexing-based wavelength modulation spectroscopy (FDM-WMS)

Journal:	*Analyst*
Manuscript ID	AN-ART-11-2018-002164.R1
Article Type:	Paper
Date Submitted by the Author:	29-Dec-2018
Complete List of Authors:	Zheng, Kaiyuan; Jilin University, College of Electronic Science and Engineering Zheng, Chuan-Tao; Jilin University, College of Electronic Science and Engineering Yao, Dan; Jilin University, College of Electronic Science and Engineering Hu, Lien; Jilin University, College of Electronic Science and Engineering Liu, Zidi; Jilin University, College of Electronic Science and Engineering Li, Junhao; Jilin University, College of Electronic Science and Engineering Zhang, Yu; Jilin University, Wang, Yi-Ding; Jilin University, College of Electronic Science and Engineering Tittel, Frank; Rice University, Electrical and Computer engineering

Journal Name

ARTICLE

Near-infrared C_2H_2/CH_4 dual-gas sensor system combining off-axis integrated-cavity output spectroscopy (OA-ICOS) and frequency-division-multiplexing-based wavelength modulation spectroscopy (FDM-WMS)

Received 00th January 20xx,
Accepted 00th January 20xx

DOI: 10.1039/x0xx00000x

www.rsc.org/

Kaiyuan Zheng,[a] Chuantao Zheng,*[a] Dan Yao,[a] Lien Hu,[a] Zidi Liu,[a] Junhao Li,[a] Yu Zhang,[a] Yiding Wang[a] and Frank K. Tittel[b]

By combining frequency division multiplexing assisted wavelength modulation spectroscopy (FDM-WMS) and off-axis integrated-cavity output spectroscopy (OA-ICOS), a near-infrared (near-IR) dual-gas sensor system was demonstrated for simultaneous chemical gas-phase detection of acetylene (C_2H_2) and methane (CH_4). Two distributed feedback (DFB) lasers modulated at the frequency of 3 kHz and 4 kHz with an emitting wavelength of 1532 and 1653 nm were used to target two absorption lines, C_2H_2 at 6523.88 cm^{-1} and CH_4 at 6046.95 cm^{-1}, respectively. A 6 cm-long cavity was fabricated, which reveals an effective path length of 9.28 m (@1532 nm, C_2H_2) and 8.56 m (@1653 nm, CH_4), respectively. Performances of the dual-gas sensor system were experimentally evaluated using C_2H_2 and CH_4 samples generated by an Environics gas mixing system. An Allan deviation of 700 parts-per-billion in volume (ppbv) for C_2H_2 with an averaging time of 200 s and 850 ppbv for CH_4 with an averaging time of 150 s were achieved for these two gas species. Dynamic measurements of C_2H_2/CH_4:N_2 mixture were performed for monitoring both C_2H_2 and CH_4 simultaneously. This dual-gas sensor has the merits of reduced size and cost compared to two separate OA-ICOS sensors and reveals the minimum detectable column density (DCD) compared to other reported C_2H_2 and CH_4 sensor systems.

1. Introduction

Chemical gas-phase analysis is significant in physics, chemistry, medical science, space science as well as in atmospheric applications [1–5]. Acetylene (C_2H_2) and methane (CH_4) are two important gas components for chemical gas-phase analysis. C_2H_2 is inflammable and explosive at ambient environment and is widely used in industry as a raw material for organic synthesis and as a dissolved gas for oil-immersed transformer analysis [6, 7]. C_2H_2 measurement is therefore important for assuring the quality of petrochemical materials and the safety in industrial production [8, 9]. CH_4 with a concentration level of ~ 1.8 parts-per-million in volume (ppmv) in the atmosphere is partially responsible for greenhouse effect [10–13]. CH_4 is also an industrial safety hazard in the coal mining industry and in the disposal of liquefied CH_4 [14–16]. Hence the development of a real-time and reliable sensor system for simultaneous monitoring C_2H_2 and CH_4 concentration level is of vital importance in atmospheric environment and industrial fields [17, 18].

In recent years, several sensing techniques with different optical schemes have been developed to deal with simultaneous multi-gas determination. In 2016, Zheng et al. developed a mid-infrared (mid-IR) CH_4/C_2H_6 sensor system at parts-per-billion by volume (ppbv) concentration levels using two distributed feedback interband cascade lasers and two miniature multi-pass cells with an effective absorption length of 54.6 m [19]. For cavity-enhanced technique, Amiot et al. demonstrated an incoherent broadband cavity-enhanced absorption spectroscopy (IBBCEAS) in the mid-IR wavelength range from 3000 to 3450 nm using an all-fiber based supercontinuum (SC) source, and C_2H_2/CH_4 detection was performed with sub-ppmv accuracy [20]. Wang et al. developed a multi-species ring-down spectrometer using near-IR continuous-wave (cw) cavity ring-down spectroscopy (CRDS) for *in-situ* measurements of CH_4 and CO_2 [21]. Photoacoustic spectroscopy (PAS) was another way for realizing multi-gas analysis. Besson et al. introduced a multi-hydrogenated compounds detection system based on a photoacoustic cell and three near-IR DFB lasers to monitor CH_4, H_2O and HCl simultaneously, and detection limits of 0.5 ppmv of CH_4, 0.2 ppmv of H_2O and 3 ppmv of HCl were achieved [22]. In 2018, a multi gas quartz-enhanced photoacoustic spectroscopy (QEPAS) sensor based on three quartz tuning forks (QTFs) with different response frequencies was proposed by Zhang et al., and detection limits at ppmv concentration levels were realized

---

[a] State Key Laboratory of Integrated Optoelectronics, College of Electronic Science and Engineering, Jilin University, 2699 Qianjin Street, Changchun 130012, China.
[b] Department of Electrical and Computer Engineering, Rice University, 6100 Main Street, Houston, TX 77005, USA
* Corresponding author. Tel.: +86-13756090979; E-mail: zhengchuantao@jlu.edu.cn (Chuantao Zheng).

for simultaneously monitoring H_2O, CH_4 and C_2H_2 by using three near-IR DFB lasers [23].

Fundamental requirements for chemical sensing and multi-gas detection are sensitivity, selectivity and affordability. Off-axis integrated-cavity output spectroscopy (OA-ICOS), a variant of integrated-cavity output spectroscopy (ICOS) meets these criteria. Compared to ICOS, the key innovation of OA-ICOS is to change the conventional on-axis alignment of the laser into an off-axis configuration to create an extremely dense-mode spectrum [24], which effectively reduces the typical amplitude noise associated with the resonant behavior of an optical cavity. Furthermore, OA-ICOS offers specificity, robustness and real-time monitoring ability for trace gas sensing.

With respect to OA-ICOS technique, previously reported sensors for multi-gas measurement were mainly in the mid-IR range [25, 26]. For multi-gas detection in the near-IR range, it is experimentally challenging due to the narrow wavelength tuning range of a near-IR laser. The combination of multiple separate sensors is a way to solve this problem. But it requires multiple data acquisition (DAQ) cards, gas cells, pressure controllers, photo detectors, lock-in amplifiers, laser current drivers and temperature controllers. This demands a large-sized vehicle for mobile deployment of these sensor units and requires high power-consumption, which deteriorates the long-term trace gas sensing characteristics.

In order to overcome these limitations, a compact dual-gas C_2H_2/CH_4 sensor system was developed by combining OA-ICOS and frequency division multiplexing (FDM) assisted wavelength modulation spectroscopy (WMS) technique. The dual-gas sensor adopted two distributed feedback (DFB) lasers operating at the wavelength of 1532 nm and 1653 nm for simultaneous detection of C_2H_2 and CH_4. A high-finesse cavity with a length of only 6 cm was implemented that provides an effective absorption path length of ~ 9 m. A LabVIEW-based FDM-WMS platform was developed for dual-gas detection using a dual-channel lock-in amplifier, a near-IR detector and a DAQ card. The sensor performances were evaluated using C_2H_2 and CH_4 samples generated by a standard gas mixing system. Such a sensor can perform the operation of driving the two DFB lasers and extracting the C_2H_2 and CH_4 harmonic signals simultaneously using a laptop and the LabVIEW platform.

2. Experimental set-up

2.1 C_2H_2/CH_4 absorption line selection

Absorption spectra of 10 ppmv C_2H_2 and 2% H_2O under a gas pressure of 760 Torr, a temperature of 300 K and an optical path length of 9.28 m are simulated using the high-resolution transmission (HITRAN) 2016 database [27], as depicted in Fig. 1(a). A C_2H_2 line centered at 1532.8 nm (6523.88 cm^{-1}) was chosen as the optimum absorption line almost with no absorption of ethane (C_2H_6) and propane (C_3H_8). In addition, the absorbance of the 10 ppmv C_2H_2 (i.e. the 1σ detection limit of the sensor) is 283 times greater than that of the 2% H_2O (i.e. a normal environmental humidity) at 1532.8 nm, thus the interference of H_2O is negligible. The DFB laser (#1) was operated at a central current of 47 mA and a temperature of 13.3 °C for C_2H_2 detection. Furthermore, an interference free CH_4 absorption line centered at 1653.7 nm (6046.95 cm^{-1}) was selected, as shown in Fig. 1(b). The absorbance of 10 ppmv CH_4 is 112 times greater than that of H_2O at 1653.7 nm, which can eliminate the influence of H_2O during the measurement. Furthermore, C_2H_6 and C_3H_8 have a flat and small absorption within this spectral region, which will not affect CH_4 detection. The absorbance of 10 ppmv CH_4 is 782 times greater than that of the 10 ppmv C_2H_6 and 930 times greater than that of the 10 ppmv C_3H_8 at 1653.7 nm. The central current of the DFB laser (#2) was set to 52 mA at 19.1 °C for CH_4 detection.

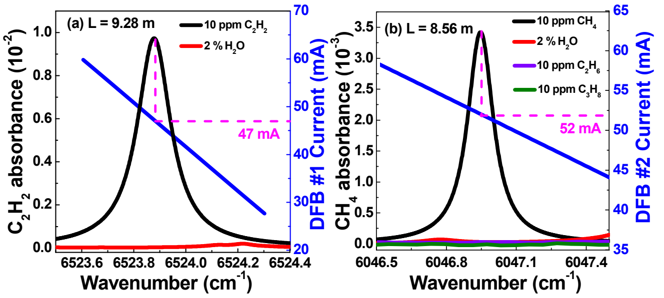

Fig. 1 (a) HITRAN simulated spectra of C_2H_2 (10 ppmv, black line) and H_2O (2%, red line) at an optical length of 9.28 m almost with no absorption of C_2H_6 and C_3H_8, and plot of the DFB laser (#1) emission wavenumber versus drive current (blue line). (b) Simulated spectra of CH_4 (10 ppmv, black line), H_2O (2%, red line), C_2H_6 (10 ppmv, purple line) and C_3H_8 (10 ppmv, green line) at an absorption length of 8.56 m as well as curve of the DFB laser (#2) emission wavenumber versus drive current (blue line).

2.2 Sensor configuration

The dual-gas OA-ICOS sensor architecture is depicted in Fig. 2. Two DFB lasers emitting single-mode radiation at the center wavelengths of 1532 nm (DFB #1, Corning Lasertron, USA) and 1653 nm (DFB #2, BL Fiber, China) were employed. Detailed parameters of the two DFB lasers are shown in Table 1. Two laser current drivers (LDC-3724B, ILX Lightwave and LDC202C, Thorlabs, USA) and two temperature controllers (TED200C, Thorlabs, USA) were used for driving laser #1 and #2, respectively. FDM-WMS technique was used for C_2H_2/CH_4 detection. For C_2H_2 detection, a scan signal (2 Hz triangular-wave) and modulation signal (3 kHz sine-wave) were generated by the LabVIEW controlled DAQ card (Model USB-6211, National Instrument, USA) to drive the DFB laser #1. For CH_4 detection, a scan signal (2 Hz triangular-wave) and modulation signal (4 kHz sine-wave) were used to drive the DFB laser #2. An fiber beam coupler (50:50 coupling ratio) was used to combine the two laser beams and an optical isolator (IO-H-1550APC, Thorlabs, USA) was used to prevent the reflected light from the cavity getting back into the laser. The combined beam was coupled into the cavity in an off-axis fashion and propagated through a 6 cm-long optical cavity formed by two mirrors with a radius of curvature (RoC) of 20 cm and a high reflectivity (R ~ 99.3–99.4%) between 1400 and 1700 nm. The cavity was equipped with an inlet and an outlet in both ends, allowing gas flow during measurements. $C_2H_2/CH_4:N_2$ mixtures were diluted from a standard 2000 ppmv C_2H_2 sample and a 1000 ppmv CH_4

sample in nitrogen (N_2) by a commercial gas mixing system (Series 4000, Environics, USA). Using an achromatic plano-convex lens with a focal length of 6 cm, the cavity output was focused onto an amplified InGaAs detector (PDA10CS, Thorlabs, USA), whose signal was digitized, analyzed, and recorded by a laptop via a DAQ card.

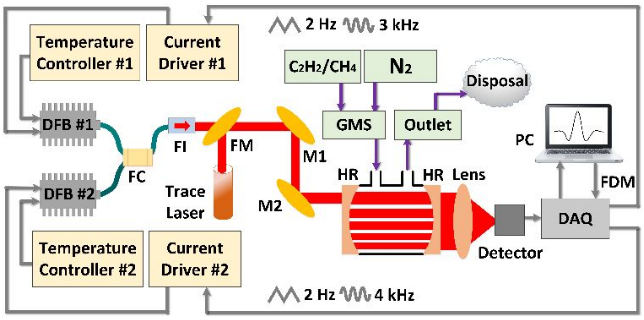

Fig. 2 Schematic diagram of the dual-gas OA-ICOS sensor system. DFB: distributed feedback laser; FC: fiber coupler; FI: fiber isolator; FM: flip mirror; M1 and M2: plane mirror; HR: highly-reflective mirror; GMS: gas mixing system; DAQ: data acquisition card; FDM: frequency division multiplexing; PC: personal computer.

Table 1 Key parameters of the DFB lasers used in C_2H_2 and CH_4 detection

DFB laser	#1	#2
Center wavelength	1532nm	1653 nm
Operating temperature	13.3 ℃	19.1 ℃
Current tuning coefficient	−0.0218 cm^{-1}/mA	−0.0708 cm^{-1}/mA
Target absorption line	6523.88 cm^{-1}	6046.95 cm^{-1}
Detection pressure	760 Torr	760 Torr
Scan frequency	2 Hz	2 Hz
Modulation frequency	3 kHz	4 kHz
Technique	FDM-WMS	FDM-WMS
Target gas	C_2H_2	CH_4

2.3. Effective path length determination

The gas absorbance (*A*) at a specific concentration level can be expressed as

$$A = -\ln (V_1 / V_2) \tag{1}$$

where V_1 and V_2 are the detector's output voltages with absorption and non-absorption at the absorption line, respectively. Based on the cavity length *d* and mirror reflectivity *R*, the effective path length *L* in OA-ICOS can be calculated by

$$L = d / (1 - R) \tag{2}$$

A triangular wave signal with a frequency of 2 Hz was used to vary the current of the two DFB lasers. Firstly, a C_2H_2 sample with a concentration level of 550 ppmv passed through the cell. The inset of Fig. 3 show the acquired C_2H_2 absorption signal as well as a fitted baseline, where V_1 and V_2 are denoted in the figure. The absorbance *A* for C_2H_2 was determined to be 0.48 using Eq. (1). Thus an absorption path length of 9.28 m was acquired as compared to the simulated data from the SpectraPlot website [28]. Then based on Eq. (2), a mirror reflectivity *R* of 99.35% was obtained. Figure 3 shows the CH_4 absorption signal acquired from 500 ppmv as well as a fitted baseline. The absorbance for CH_4 is 0.154, resulting in an absorption path length of 8.56 m and a calibrated mirror reflectivity of 99.3%. Consequently, two absorption path lengths of 9.28 m and 8.56 m were obtained in one cavity for C_2H_2 and CH_4 detection, respectively.

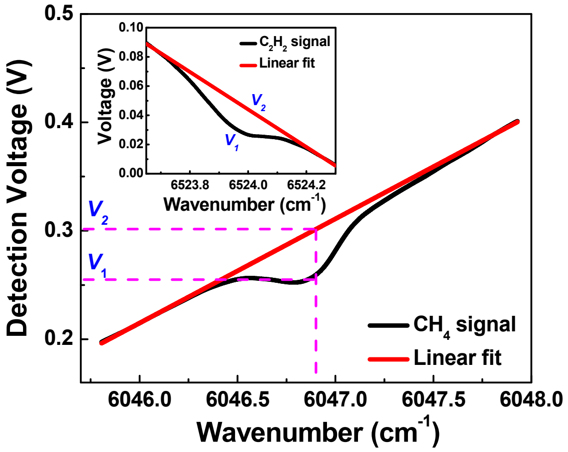

Fig. 3 Absorption spectrum (black line) with fitted baseline (red line) for effective path length determination of CH_4 and C_2H_2 (inset figure) detection, respectively

2.4. LabVIEW-based FDM-WMS technique

Data sampling and processing of the FDM-WMS technique were realized on a LabVIEW-based platform, and the function diagram is shown in Fig. 4. A scan signal (2 Hz, triangular-wave) and two modulation signals (ω_1: 3 kHz and ω_2: 4 kHz, sine-wave) are generated by the modulation-signal array, which are supplied to a digital-to-analog converter (DAC) module and then applied to the two DFB lasers (#1 and #2) separately via the DAQ card. The detector output signal with different modulation frequency was sampled via an analog-to-digital converter (ADC) module of the DAQ card. The output signal from the ADC module was split into two parts, one (ω_1) was for C_2H_2 measurement and the other (ω_2) was for CH_4 detection. Demodulation of the sensing signals with different frequencies was realized using a LabVIEW-based dual-channel lock-in amplifier. The two split signals as well as two frequency-doubled orthogonal signals synchronized by the modulation signal were sent to each lock-in amplifier channel for second harmonic (2*f*) signal extraction. The sampling rate of the DAC module is required to be the same with the ADC, which was essential for lock-in data-processing. For further data processing, a "R" signal with a positive bias was generated and the baseline was removed from the "R" signal by a subtraction operation. Finally the 2*f* signal biased at zero was extracted to determine the C_2H_2/CH_4 gas concentration simultaneously.

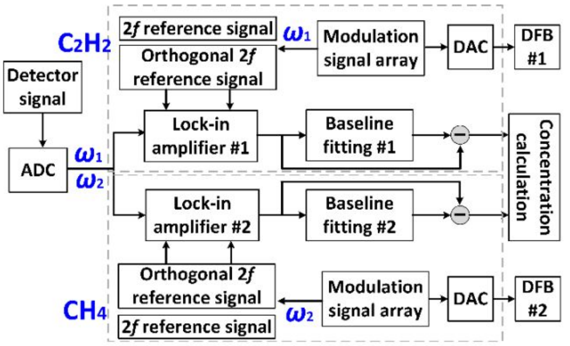

Fig. 4 Function diagram of the LabVIEW-based FDM-WMS platform with a dual-channel lock-in amplifier. ADC: analog-to-digital converter; DAC: digital-to-analog converter.

2.5. Modulation depth optimization

In 2*f*-WMS, the optimal modulation depth is theoretically 2.2 times of the half width at half maximum (HWHM) of the gas absorption line [29, 30]. To determine the optimum modulation amplitude, 2*f* signal amplitudes of 400 ppmv C_2H_2 measured at different modulation amplitude are shown in Fig. 5(a). The maximum amplitude is observed at a modulation amplitude of ~ 0.3 V with a modulation coefficient of 0.13/0.062 = 2.1. Furthermore, a 500 ppmv CH_4 sample was used to optimize the modulation depth for CH_4 detection, as depicted in Fig. 5(b). An optimum modulation amplitude of 0.09 V was selected, leading to a modulation coefficient of 0.125/0.058=2.15.

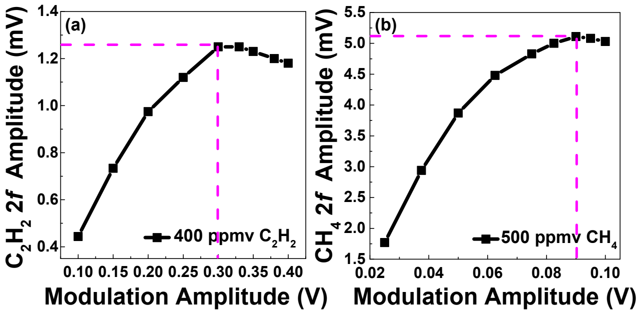

Fig. 5 Measured amplitude of the 2*f* signal versus the modulation amplitude for (a) a 400 ppmv C_2H_2:N_2 mixture and (b) a 500 ppmv CH_4:N_2 mixture, respectively.

3. Results and discussion

3.1. Experimental details

The wavelength scan signal of the two DFB lasers was a trigonometric signal with a frequency of 2 Hz. A peak-to-peak amplitude of 1.5 V yielded a current range of 28–58 mA (20 mA/V) for laser #1 and 38–68 mA for laser #2, respectively. With the FDM-WMS method, the sine-wave modulation signal for DFB laser #1 possessed a frequency of 3 kHz and a peak-to-peak amplitude of 0.3 V. For DFB laser #2, the modulation signal was a sinusoidal signal of 4 kHz with an optimum amplitude of 0.09 V. Based on the LabVIEW platform with a data sampling rate of 100 kHz, one absorption signal was obtained per 2 s including the sampling time and the data processing time.

3.2. C_2H_2 sensing performance

Different C_2H_2 samples balanced with pure N_2 (0, 200, 400, 600 and 800 ppmv) were generated by an Environics gas mixing system for sensor calibration. The 2*f* signals for different C_2H_2 concentration levels from 100 to 800 ppmv are shown in Fig. 6. Figure 7 demonstrates the maximum amplitude of the 2*f* signal for each concentration level with a ~ 3 min observing time. As shown in the inset of Fig. 7, the acquired fitting equation between the C_2H_2 concentration (*C*, in ppmv) and the 2*f* signal amplitude (max (2*f*), in mV) is

$$C = 402.55 \times \max(2f) - 100.64 \qquad (3)$$

An Allan-Werle analysis was performed to evaluate the long-term stability and precision of the sensor system. The C_2H_2 concentration level was measured in pure N_2 atmosphere over a period of ~ 50 min, and plot of the Allan deviation as a function of averaging time is shown in Fig. 8. The Allan deviation yields a precision of 10.2 ppmv with a 2 s averaging time and also shows an optimum averaging time of 200 s corresponding to a detection limit of 700 ppbv. As the averaging time increases, the Allan-Werle plot continuously decreases similar to the decrease of the curve of ~1/√*t*, indicating a white-noise dominated sensor system with a < 300 s integration time.

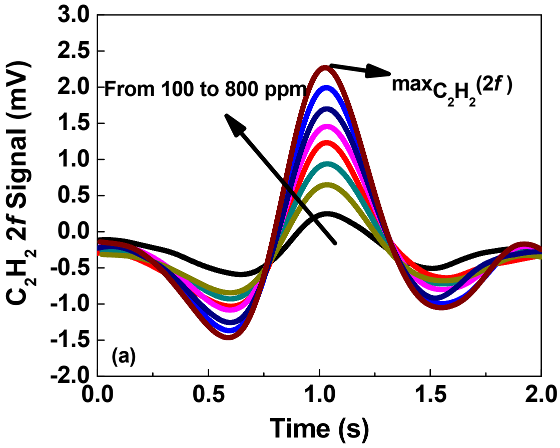

Fig. 6 The recorded 2*f* signal for eight C_2H_2 concentration levels from 100 to 800 ppmv in a step of 100 ppmv. The modulation frequency was 3 kHz.

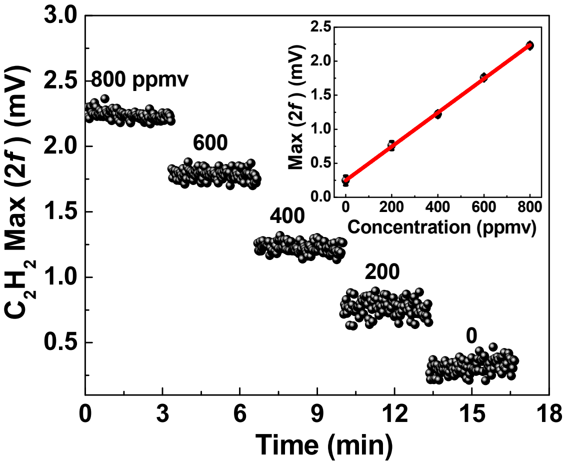

Fig. 7 The measured max (2*f*) at different C_2H_2 concentration levels and the inset is the fitting curve of the relationship between C_2H_2 concentration and max (2*f*).

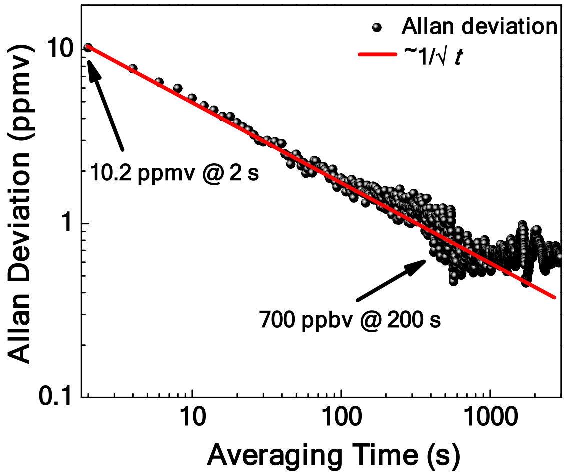

Fig. 8 Curve of the Allan deviation versus the average observing time based on the measured C_2H_2 concentration levels in N_2 atmosphere during ~ 50 min period.

3.3. CH_4 sensing performance

Figure 9 shows the recorded 2*f* signals at seven different CH_4 concentration levels of 0, 100, 200, 300, 400, 500 and 1000 ppmv. The measured amplitudes over a calibration time period of ~ 3 min for different CH_4 concentration levels (0, 100, 200, 300, 400 and 500 ppmv) are shown in Fig. 10. The inset of Fig. 10 shows the relation between the averaged 2*f* absorption signal (max (2*f*), in mV) and the CH_4 concentration (*C*, in ppmv). This relationship is fitted by a linear curve as

$$C = 101.04 \times \max(2f) - 13.52 \quad (4)$$

Measurements of the CH_4 sample under pure N_2 atmosphere over a period of ~ 50 min were subsequently carried out. As shown in Fig. 11, a detection limit of 14 ppmv is achieved based on an Allan deviation analysis for an averaging time of 2 s, which can be further improved to 850 ppbv with an averaging time of 150 s. The Allan deviation decreases with the increase of the averaging time before the system drift starts to dominate, indicating that a white-noise dominated sensor with a < 250 s integration time was achieved for CH_4 detection.

With respect to the origin of the oscillatory behavior in Fig. 8 after 300 s and in Fig. 11 after 250 s, it is mainly dominated by system drift, which could be composed of the DFB laser's drift, the electronic components' temperature drift, the optical fringe and etalon effect in the optical alignment, and the instability of the detector and the dilution system due to long-term operation.

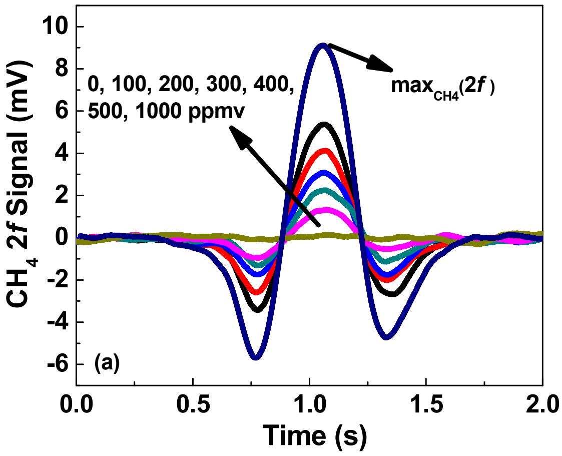

Fig. 9 The recorded 2*f* signal at seven different CH_4 concentration levels of 0, 100, 200, 300, 400, 500 and 1000 ppmv. The modulation frequency was set at 4 kHz.

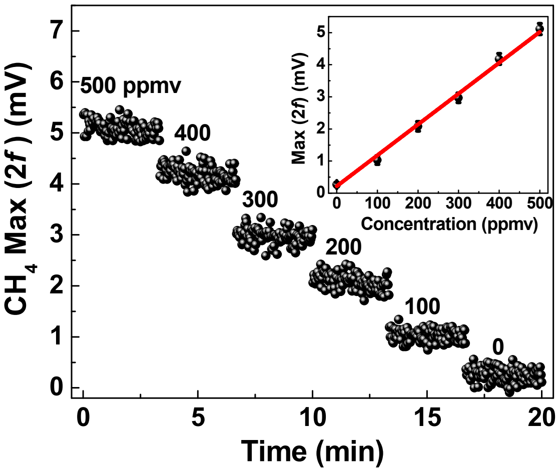

Fig. 10 Measured max (2*f*) versus calibration time at different CH_4 concentration levels. Inset is the fitting curve of the relationship between CH_4 concentration and max (2*f*).

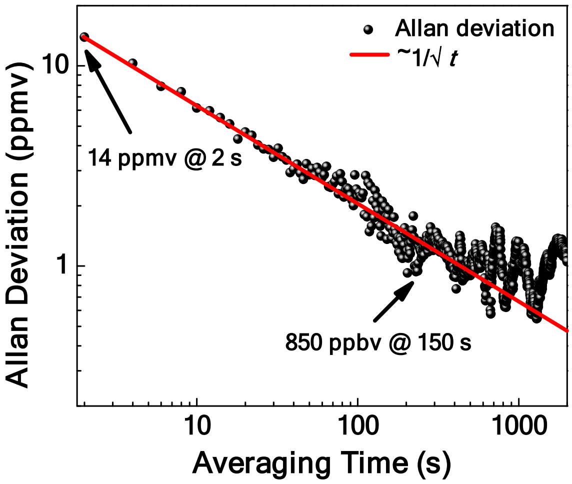

Fig. 11 Allan deviation plot of the sensor system based on the ~50 min concentration measurement results for the CH_4 sample in N_2 atmosphere.

3.4. Dual-gas sensing performance

As shown in Fig. 12, the dynamic performance of the dual-gas sensor was further assessed using three CH_4 samples (1000, 500 and 0 ppmv) generated by an Environics gas mixing system (GMS) and the standard 2000 ppmv C_2H_2 sample. Two valves were used to switch between CH_4 and C_2H_2 gas streams into the gas cell, as shown in Fig. 12(c). Figure 12(a) depicts the measured CH_4 and C_2H_2 concentration results during the three gas stream exchanges. A detailed description of the measurement results during the first gas stream exchange is shown in Fig. 12(b). A response time of ~ 78 s is determined to complete the exchange at a gas flow rate of ~ 300 standard cubic centimeter per minute (sccm). These results exhibit the normal operation of the dual-gas sensor system for monitoring both C_2H_2 and CH_4 simultaneously.

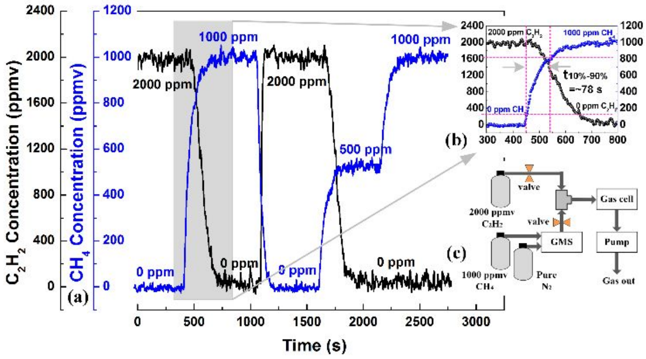

Fig. 12 (a) $C_2H_2/CH_4:N_2$ concentration measurements using the dual-gas sensor system. (b) Detailed description of the measured concentration during the first switch between C_2H_2 and CH_4 streams. (c) Schematic diagram of a C_2H_2/CH_4 mixing set-up using the CH_4 sample generated by the gas mixing system (GMS) and a standard 2000 ppmv C_2H_2 sample.

3.5. Comparison and discussion

As shown in Table 2, the performances of the dual-gas sensor system using FDM-WMS and OA-ICOS for C_2H_2 detection are compared with those of previously reported sensors [20, 23, 31-34] using IBBCEAS, QEPAS, tunable diode laser absorption spectroscopy (TDLAS), multi-pass cell (MPC) based WMS and OA-ICOS techniques. Table 3 demonstrates the comparison between the CH_4 detection performance of this sensor system and those of previously reported sensors [35-39] using CRDS, hollow-core photonic bandgap fiber (HC-PBF), TDLAS, MPC-WMS and OA-ICOS.

For the above reported techniques, the detection sensitivity is primarily determined by the absorption path length (or effective absorption path length). Though there are differences in sensitivity and absorption path length, a sensor system can be characterized by the detectable column density (DCD, ppmv·m), which represents the noise level of the sensor system. It can be found from Table 2 and Table 3 that with an acceptable averaging time (150 s and 200 s), the proposed sensor system possesses the minimum DCD, indicating the lowest noise level of the sensor by combining the FDM-WMS and OA-ICOS. An obvious advantage of the FDM-WMS technique is that the 1/*f* laser excess noise and baseline slope can be suppressed by optimizing the modulation depth and using lock-in processing. Also, the off-axis configuration as well as the high-finesse cavity made the sensor more stable and robust, and a long absorption path length and high sensitivity can be achieved. The fabricated miniature cavity with a length of only 6 cm provides an absorption path length up to ~ 9 m, which makes such sensor more suitable for field and portable deployment as compared to other kinds of sensor systems. In addition, by using higher reflectivity dielectric mirror and increasing the cavity length, the reported OA-ICOS sensor system can easily achieve an obvious increase of effective absorption path length (to ~ km level), leading to a significant enhancement in sensitivity (to ~ ppbv level).

Table 2 Comparison among the performance of this sensor for C_2H_2 detection and those of other reported devices in Refs. [31–34]. DCD: Detectable column density; L_{eff}: Effective absorption path length; LoD: Limit of detection.

Refs.	Technique	Laser source	L_{eff} (m)	DCD (ppmv·m)	Averaging time (s)
[20]	IBBCEAS	3-3.45 μm SC	300	150	900
[23]	QEPAS	1.533 μm DFBL	/	5 ppmv (LoD)	1
[31]	TDLAS	1.53 μm DFBL	0.15	30	30
[32]	TDLAS	1.53 μm DFBL	0.06	23.5	7.5
[33]	MPC-WMS	1.53 μm DFBL	20	80	2
[34]	OA-ICOS	1.53 μm DFBL	367	7.34	300
This paper	OA-ICOS & FDM-WMS	1.53 μm DFBL	9.28	6.4	200

Table 3 Comparison among the performance of this sensor for CH_4 detection and those of other reported devices in Refs. [35–39]. DCD: Detectable column density; L_{eff}: Effective absorption path length; DL: Diode laser

Refs.	Technique	Laser source	L_{eff} (m)	DCD (ppm v·m)	Averaging time (s)
[35]	CRDS	1.65 μm DFBL	2600	135	900
[36]	HC-PBF	1.65 μm DFBL	5.1	51	570
[37]	MPC-WMS	1.65 μm DFBL	30	25.2	5
[38]	TDLAS	1.65 μm DFBL	0.4	12	1
[39]	OA-ICOS	1.65 μm DL	5000	10	676
This paper	OA-ICOS & FDM-WMS	1.65 μm DFBL	8.56	7.2	150

4. Conclusions

A sensitive and selective sensor system using two DFB lasers was demonstrated for simultaneous C_2H_2 and CH_4 detection by combining OA-ICOS and FDM-WMS technique. An ultra-compact absorption cell with two different effective optical path length of 9.28 m for C_2H_2 detection and 8.56 m for CH_4 detection was used to enhance gas absorption. The sensor system was first evaluated for individual C_2H_2 and CH_4 detection. An Allan deviation analysis yielded a detection sensitivity of 700 ppbv for C_2H_2 with an averaging time of 200 s and a detection sensitivity of 850 ppbv for CH_4 with an averaging time of 150 s. Subsequently, the sensor system was evaluated for simultaneously dual-gas detection using the C_2H_2/CH_4 mixing set-up. The demonstrated dual-gas sensor architecture shows the advantages of simultaneous C_2H_2/CH_4 detection with a single sensor system of reduced size and cost without affecting sensitivity, selectivity and reliability.

Conflicts of interest

There are no conflicts to declare.

Acknowledgements

The National Key R&D Program of China (No. 2017YFB0405300), National Natural Science Foundation of China (Nos. 61775079, 61627823), Key Science and Technology R&D program of Jilin Province, China (No. 20180201046GX), Industrial Innovation Program of Jilin Province, China (No. 2017C027), and the National Science Foundation (NSF) ERC MIRTHE award and Robert Welch Foundation (No. C-0586).

Notes and references

1 H. P. Wu, L. Dong, H. D. Zheng, Y. J. Yu, W. G. Ma, L. Zhang, W. B. Yin, L. T. Xiao, S. T. Jia, and F. K. Tittel, *Nat. Commun.*, 2017, **8**, 15331–15338.

2 K. Y. Zheng, C. T. Zheng, Y. Zhang, Y. D. Wang, and F. K. Tittel, *Sensors*, 2018, **18**, 3646–3670.

3 W. Jin, Y. Cao, F. Yang, and H. L. Ho, *Nat. Commun.*, 2015, **6**, 7767–7775.

4 K. W. Anthony, R. Daanen, P. Anthony, T. S. V. Deimling, C. L. Ping, J P. Chanton, and G. Grosse, *Nat. Geosci.*, 2016, **9**, 679–682.

5 K. Y. Zheng, C. T. Zheng, Z. D. Liu, Q. X. He, Q. L. Du, Y. Zhang, Y. D. Wang, and F. K. Tittel, *Analyst*, 2018, **143**, 4699–4706.

6 J. S. Li, G. Durry, J. Cousin, L. Joly, B. Parvitte, and V. Zeninari, *J. Quant. Spectrosc. Radiat. Transf.*, 2010, **111**, 2332–2340.

7 Y. Cao, W. Jin, H. L. Ho, L. Qi, and Y. H. Yang, *Appl. Phys. B*, 2012, **109**, 359–366.

8 K. Y. Zheng, C. T. Zheng, Q. X. He, D. Yao, L. E. Hu, Y. Zhang, Y. D. Wang, and F. K. Tittel, *Opt. Express*, 2018, **26**, 26205–26216.

9 G. M. Ma, S. J. Zhao, J. Jiang, H. T. Song, C. R. Li, Y. T. Luo, and H. Wu, *Sci. Rep.*, 2017, **23**, 3435–3442.

10 C. T. Zheng, W. L. Ye, N. P. Sanchez, C. G. Li, L. Dong, Y. D. Wang, R. J. Griffin, and F. K. Tittel, *Sens. Actuators B: Chem.*, 2017, **244**, 365–372.

11 I. J. Simpson, F. S. Rowland, S. Meinardi, and D. R. Blake, *Geophys. Res. Lett.*, 2006, **33**, L22808.

12 B. Heiko, G. F. France, G. T. Charles, R. S. Clare, J. E. Tim, M. Ian, S. Anatoly, N. Sten, S. Anatoly, O. Alexander, and S. Christiane, *Geophys. Res. Lett.,* 2005, **32**, L14709.

13 C. T. Zheng, W. L. Ye, G. L. Li, X. Yu, C. X. Zhao, Z. W. Song, and Y. D. Wang, *Sens. Actuators B: Chem.*, 2011, **160**, 389–398.

14 L. Dong, J. Wright, B. Peters, B. A. Ferguson, F. K. Tittel, and S. McWhorter, *Appl. Phys. B-Lasers Opt.*, 2012, **107**, 459–467.

15 J. Leis, D. Buttsworth, C. Snook, and G. Holmes, *IEEE Trans. Instrum. Meas.*, 2014, **63**, 3088–3095.

16 M. Triki, T. N. Ba, and A. Vicet, *Infrared Phys. Technol.*, 2015, **69**, 74–80.

17 M. Kohring, S. Huang, M. Jahjah, W. Jiang, W. Ren, U. Willer, C. Caneba, L. Yang, D. Nagrath, W. Schade, and F. K. Tittel, *Appl. Phys. B-Lasers Opt.*, 2014, **117**, 445–451.

18 W. Ren, L. Luo, and F. K. Tittel, *Sens. Actuators B: Chem.*, 2015, **221**, 1062–1068.

19 C. T. Zheng, W. L. Ye, N. P. Sanchez, A. K. Gluszek, A. J. Hudzikowski, C. G. Li, L. Dong, R. J. Griffin, and F. K. Tittel, *IEEE Photonic. Tech. Lett.*, 2016, **28**, 2351–2354.

20 C. Amiot, A. Aalto, P. Ryczkowski, J. Toivonen, and G. Genty, *Appl. Phys. Lett.*, 2017, **111**, 061103.

21 C. Wang, N. Srivastava, B. A. Jones, and R. B. Reese, *Appl. Phys. B-Lasers Opt.*, 2008, **92**, 259–270.

22 J. Besson, S. Schilt, and L. Thévenaz, *Spectrochimica Acta Part A*, 2004, **60**, 3449–3456.

23 Q. D. Zhang, J. Chang, Z. H. Cong, J. C. Sun, and Z. L. Wang, *IEEE Photonic. J.*, 2018, **10**, 6804308.

24 J. G. Anderson, J. B. Paul, and L. Lapson, *Appl. Opt.*, 2001, **40**, 4904–4910.

25 D. D. Arslanov, K. Swinkels, S. M. Cristescu, and F. J. M. Harren, *Opt. Express*, 2011, **19**, 24078–24089.

26 L. Han, H. Xia, T. Pang, Z. R. Zhang, B. Wu, S. Liu, P. S. Sun, X. J. Cui, Y. Wang, M. W. Sigrist, and F. Z. Dong, *Infrared Phys. Technol.*, 2018, **91**, 37–45.

27 I. E. Gordon, L. S. Rothman, C. Hill, R. V. Kochanov, Y. Tan, P. F. Bernath, M. Birk, V. Boudon, A. Campargue, *et al.*, *J. Quant. Spectrosc. Radiat. Transf.*, 2017, **203**, 3–69.

28 http://www.spectraplot.com/absorption

29 K. Liu, T. G. Liu, J. F. Jiang, G. D. Peng, H. X. Zhang, D. G. Jia, Y. Wang, W. Jing, and Y. Zhang, *J. Lightwave Technol.*, 2011, **29**, 15–21.

30 W. L. Ye, C. G. Li, C. T. Zheng, N. P. Sanchez, A. K. Gluszek, A. J. Hudzikowski, L. Dong, R. J. Griffin, and F. K. Tittel, *Opt. Express*, 2016, **24**, 16973–16985.

31 Q. X. He, C. T. Zheng, H. F. Liu, B. Li, Y. D. Wang, and F. K. Tittel, *Infrared Phys. Technol.*, 2016, **75**, 93–99.

32 S. Wagner, M. Klein, T. Kathrotia, U. Riedel, T. Kissel, A. Dreizler, and V. Ebert, *Appl. Phys. B*, 2012, **107**, 585–589.

33 M. Dong, C. T. Zheng, D. Yao, G. Q. Zhong, S. Z. Miao, W. L. Ye, Y. D. Wang, and F. K. Tittel, *Opt. Express*, 2018, **26**, 12081–12091.

34 L. D. Le, J. D. Tate, M. B. Seasholtz, M. Gupta, T. Owano, D. Baer, T. Knittel, A. Cowie, and J. Zhu, *Appl. Spectrosc.*, 2008, **62**, 59–65.

35 B. L. Fawcett, A. M. Parkes, D. E. Shallcross, and A. J. Orrewing, *Phys. Chem. Chem. Phys.*, 2002, **4**, 5960–5965.

36 A. M. Cubillas, J. M. Lazaro, O. M. Conde, M. N. Petrovich, and J. M. Lopez-Higuera, *Sensors*, 2009, **9**, 6261–6272.

37 D. Stachowiak, P. Jaworski, P. Krzaczek, G. Maj, and M. Nikodem, *Sensors*, 2018, **18**, 529–540.

38 B. Li, C. T. Zheng, H. F. Liu, Q. X. He, W. L. Ye, Y. Zhang, J. Q. Pan, and Y. D. Wang, *Sens. Actuators B: Chem.*, 2016, **225**, 188–198.

39 W. Gulzow, G. Rehder, B. Schneider, J. S. V. Deimling, and B. Sadkowiak, *Limnol. Oceanogr. Meth.*, 2011, **9**, 176–184.

A near-infrared C_2H_2/CH_4 sensor was demonstrated utilizing a miniaturized high finesse cavity with high sensitivity and remarkable dynamic measurement performance